POLITECNICO DI TORINO
Repository ISTITUZIONALE

Cobalt-Based Metallic Glass Microfibers for Flexible Electromagnetic Shielding and Soft Magnetic Properties

(Article begins on next page)

20 May 2024

Cobalt-Based Metallic Glass Microfibers for Flexible Electromagnetic Shielding and Soft Magnetic Properties

Elham Sharifikolouei,* Tomasz Kozieł, Piotr Bała, Antoni Żywczak, Łukasz Gondek, Reza Rashidi, Michela Fracasso, Roberto Gerbaldo, Gianluca Ghigo, Laura Gozzelino, and Daniele Torsello

Thin and flexible materials that can provide efficient electromagnetic interference (EMI) shielding are urgently needed, particularly those that can be rapidly processed and withstand harsh environments. Cobalt-based metallic glasses stand out as prime candidates due to their excellent soft magnetic properties, satisfactory shielding features, and mechanical properties. Herein, a recently developed technique is used to fabricate metallic glass microfibers from $Co_{66}Fe_4Mo_2Si_{16}B_{12}$ alloy. The produced microfibers are characterized for their size and uniformity by scanning electron microscopy and their amorphous structure is confirmed by X-ray diffraction (XRD) and differential scanning calorimetry (DSC). The cobalt-based metallic glass microfibers show an EMI shielding factor that reaches five in the static regime and obtains an up to 25-fold increase of the attenuation constant in the Ku frequency band. This performance originates from the combination of soft magnetic properties and excellent electrical conductivity. In addition, the flexible microfibers exhibit excellent hardness and elasticity making them suitable for EMI shielding of complex geometries. Their hardness and elastic modulus are measured by nanoindentation to be 11.31 ± 0.60 GPa, and 110.54 ± 11.24 GPa, respectively.

1. Introduction

Cobalt-based amorphous alloys, commonly referred to as metallic glasses, have attracted a great deal of attention due to their extraordinary properties like soft magnetic characteristics, low magnetostriction value, coercivity and hysteresis loss, high corrosion and wear resistance, and high strength,[1] which make them a promising candidate for industrial applications.[2,3] Notably, when juxtaposed with other amorphous soft magnetic materials, Co-based metallic glasses demonstrate elevated complex permeability even at higher frequencies, exhibiting an advanced frequency threshold of Snoek's limit, enhancing their suitability for microwave absorption.[4] The Co—Fe—B—Si—Nb system showcases commendable soft magnetic properties such as a peak saturation magnetization of 0.72 T, low coercive force within 0.2–0.5 A/m, high permeability of 47 165 at 1 KHz, as well as excellent mechanical properties with super high fracture strength of 2980–3600 MPa and Young's modulus of 121–166 GPa.[5][6] This system also presents promising corrosion resistance.[4] The composition of $Co_{66}Fe_4Mo_2Si_{16}B_{12}$ closely mirrors the commercially prevalent alloy, vitrovac 6025X, an amorphous metallic ribbon manufactured by Vacuumschmelze GmbH. It is widely used as an ideal material for magnetic heads, magnetic field sensors, chokes, transformers, and electronic article surveillance tags thanks to its very high static magnetic

E. Sharifikolouei, R. Rashidi, M. Fracasso, R. Gerbaldo, G. Ghigo,
L. Gozzelino, D. Torsello
Institute of Materials Physics and Engineering
Department of Applied Science and Technology
Politecnico di Torino (POLITO)
Torino Italy
E-mail: elham.sharifikolouei@polito.it

T. Kozieł, P. Bała
Faculty of Metals Engineering and Industrial Computer Science
AGH University of Krakow
Kraków Poland

P. Bała, A. Żywczak
Academic Centre for Materials and Nanotechnology
AGH University of Krakow
Kraków Poland

Ł. Gondek
Faculty of Physics and Applied Computer Science
AGH University of Krakow
Kraków Poland

M. Fracasso, R. Gerbaldo, G. Ghigo, L. Gozzelino, D. Torsello
Istituto Nazionale di Fisica Nucleare
Sezione di Torino
Torino Italy

ADVANCED
SCIENCE NEWS

www.advancedsciencenews.com

ADVANCED
ELECTRONIC
MATERIALS
Open Access

www.advelectronicmat.de

permeability (μ_i > 100 000), high thermal stability of magnetic permeability, and very low magnetic losses, with a saturation induction (Bs) of 0.58 T.[2] Since the material is amorphous, it is possible to modify and improve the soft magnetic properties of vitrovac (the hysteresis loop shape) by inducing uniaxial magnetic anisotropy, e.g., thermal annealing under crystallization temperature in the presence of the magnetic field.[7] This is indeed one of the main advantages of amorphous metals for the fabrication of magnetic sensors to have control over the hysteresis loop. Kekalo et al.[8] investigated the $Co_{70}Fe_5Si_{15}B_{10}$ ($\lambda_s \approx 10^{-6}$) alloy for its potential in electronic devices characterized by a low magnetic-noise level. Their findings suggest that magnetization manifests through modest Barkhausen jumps in the presence of a weak applied field. As this field intensifies, the jumps become more pronounced, but in the final stages, the magnetization exhibits only slight Barkhausen jumps. Furthermore, given the substantial magnetic permeability and minimal saturation magnetostriction of the Co-based alloys,[9,10] vitrovac is also a promising candidate for magnetic shielding applications. The underlying reason for its pronounced soft magnetic properties can be traced back to Co-based grains, ranging between 2 and 20 nm, which are encapsulated within an amorphous Fe-rich matrix. Magnetic softening due to nanocrystallization was reported by Aguilarsahagun et.al.[11] and Betancourt et.al.[12] for the following compositions: $Co_{66}Fe_4Mo_2Si_{16}B_{12}$, $Co_{66}Fe_4Mo_2Si_{16.5}B_{11.5}$, and $Co_{66}Fe_4Ni_1Si_{15}B_{14}$.[13,14] The exceptional soft magnetic properties observed in both amorphous and nanocrystalline alloys are anchored in the magnetic exchange interaction length. In these instances, this length exceeds the grain size within the alloy, culminating in an average magnetocrystalline anisotropy. It's imperative to highlight that the magnetic interactions in vitrovac (or alloys with analogous compositions) are decidedly more intricate than those in Fe-based nanocrystalline alloys, primarily due to the incorporation of Co, Co2B, and Co3B crystalline phases.[13,14] Swierczek et al.[15] have indicated that annealing $Co_{71}Fe_1Mo_1Mn_4Si_{14}B_9$ beyond its crystallization temperature results in increased magnetic hardness. Concurrently, traditional heating techniques applied to the amorphous vitrovac 6025X lead to its augmented softening in its amorphous phase. This softening could potentially be attributed to the enlargement of atomic medium-range order domains.

With the emergence of next-generation flexible electronics, a wide range of applications are introduced such as flexible display technologies, textiles, wearable electronics, energy harvesting devices, and health monitoring sensors. While conventional electronics are very capable of these functions, flexible electronics are intended to expand the mechanical features to adhere to novel form factors. Conductive polymer composites (CPCs) are a popular class of materials for flexible EMI shielding thanks to their high conductivity, corrosion resistance, and lightweight. They are often composed of polymer and high-conductive fillers.[16–18] Carbon-filled polymer composites (e.g., graphene, carbon nanotube) achieved EMI shielding of 20.2 dB with minimal loading of MWCNT and graphite nanoplatelets reported by Khatua et al.[19] and 45.1 dB with 3.47 vol% of reduced graphene oxides according to Li et al.[20] However, the EMI shielding efficiency requires to be improved further. Another popular conductive filler is metals. Metals are excellent conductors of electricity and show promise for electromagnetic interference (EMI) shielding due to

their high electrical conductivity Liu et al.[21] have reported the fabrication of Ni/Cu/MG (Metallic Glass) multilayer composite through a two-step electroless plating process. This composite exhibited exemplary EMI shielding, registering an SE of 35 dB and an impressive SE/t of 1750 dB mm^{-1} at a mere 0.02 mm thickness. Additionally, this highly flexible composite has shown a strong tensile strength of 1.2 GPa and exceptional bending stability. However, metal-filled CPCs have drawbacks including corrosion, high density, and cost, and achieving sufficient EMI shielding requires incorporating a large amount of metallic fillers, surpassing the percolation limit. This high percolation not only increases density and cost but also reduces product processability and mechanical reliability.[18]

Metallic glasses, distinguished by their absence of grain boundaries and disordered atomic structure, offer a unique combination of properties including high strength, exceptionally soft magnetic characteristics, elevated corrosion and wear resistance, as well as high electrical conductivity. These attributes form a comprehensive package of properties, some of which are typically lacking in conventional alloys. One of the challenges hindering their full utilization in the field of microelectronics is the associated costs and difficulties in casting them in bulk forms, and in the field of flexible electronics, they are mostly used in the form of melt-spun ribbons. Our recent innovation has introduced a novel technique for producing metallic glasses in the form of microfibers. This approach opens up possibilities for utilizing metallic glasses in flexible electronics, where they can be easily shaped, and woven into cellular structures, bundles, textiles, and smart sensors.[22,23] Leveraging their flexibility, magnetic microfibers can be employed to construct magnetic weaves for shields.[3] Furthermore, their unique microstructure and size effects confer excellent structural and functional properties.[24,25] While significant research has focused on fabricating metallic glass nanofibers for microelectronics applications, the exploration of metallic glass microfibers remains relatively underexplored.

Several studies have reported the fabrication of metallic glass nanowires with diameters ranging from 50 to 2000 nm using gas atomization.[26] Additionally, chemical reduction methods have been employed to create metallic glass nanostructures varying in size from 2 nm to several 100 nm.[27,28] When it comes to fabricating metallic glass microfibers, the prevailing method uses a force-driven strategy. where a metallic glass master alloy (rod) is rapidly heated into its supercooled liquid state, and the applied force induces microscale metallic glass microfibers through superplastic deformation of the metallic glass.[25] Similarly, another promising method to fabricate glass-coated metallic glass microwires is through the Taylor–Ulitovski technique. In this technique, a few grams of a desired composition master alloy are melted in a Pyrex-like glass tube using high-frequency induction heating. The molten metal is encased in the softened glass, forming a droplet. A glass capillary is drawn from the softened glass, and as the molten metal fills it, a microwire with a glass shell around the metal core is created. The process continuously feeds glass into the heating zone while the initial alloy quantity limits the core size.[29] Zhukova et al. have used this technique to fabricate Co-rich ultra-thin glass-coated amorphous wires with the composition of $Co_{67.05}Fe_{3.84}Ni_{1.44}Si_{14.47}B_{11.51}Mo_{1.69}$ which has shown considerable GMI ratio is at higher frequencies. Although at

conventional frequency f = 10 MHz, the Giant magneto impedance (GMI) ratio has shown to be ≈60%.[30] The same technique was used to fabricate numbers of other Co-rich and Fe-rich soft magnetic microwires.[31–34] There are numerous advantages to this technique including the control over parameters, the ability to form continuous microwires even up to 10 000 m, and the repeatability of the technique for scaled-up processes; however, the casting rate of this technique is limited by the ability of the metal to follow the moving glass. Besides, the glass coating around the microwire limits its application in wearable electronics when the conductivity of the microwire is required.

In this work, we have used a recently developed technique by Sharifikolouei et al.[35,36] to fabricate metallic glass microfibers from $Co_{66}Fe_4Mo_2Si_{16}B_{12}$ in a single-step process. The same technique has recently been utilized to fabricate Fe-based soft magnetic metallic glass microfibers displaying anisotropic static field shielding behavior that corresponded to their anisotropic nature, with the best shielding performance observed when the magnetic field was aligned with the microfibers. Embedding the microfibers in a composition structure resulted in a 20–25 times increase in the composite's attenuation constant at GHz frequencies.[37] Here, the Co-based metallic glass system with higher magnetic permeability and better mechanical properties is selected to be fabricated in the form of microfibers. The resulting metallic glass microfibers are in the range of 2–20 µm in diameter with lengths from several mm to 1000 mm. We focus on the full characterization of their magnetic properties and their potential as electromagnetic shielding materials in both static and high-frequency regimes.

2. Experimental Section

2.1. Microfibers Fabrication

The $Co_{66}Fe_4Mo_2Si_{16}B_{12}$ (Co, Fe, Mo, Si, and B > 99.9%purity) alloy ingots were synthesized by Arc Melter (Edmund Bühler GmbH) under Ti-gettered argon atmosphere. To reach homogenous compositions, ingots were re-melted four times. The ingots were suction-casted in a copper mold with a water-cooled system to produce rods. The rods were further used to fabricate $Co_{66}Fe_4Mo_2Si_{16}B_{12}$ microfibers through a modified melt-spinning (Edmund Bühler GmbH) technique. The technique was explained in more detail by Sharifikolouei et al.[35] Similar to the standard melt-spinning technique, the rod was molten by an induction coil in a BN crucible (18 × 95 mm). The melt was ejected droplet by droplet on a rotating copper wheel (V = 60 m^{-1} s) through a rectangular slit nozzle (10 × 0.03 mm^2) (INNOVACERA, China) by applying the argon gas pressure on the melt (1500 mbar) in an argon-filled chamber (400 mbar). The distance between the slit nozzle and the rotating wheel was fixed at 150 µm.

2.2. Microfibers Characterization

Microstructure analysis was conducted by scanning electron microscopy (SEM) equipped with energy-dispersive spectroscopy. The crystallographic structure was investigated by X-ray diffraction with a PANalytical Empyrean X-ray diffractometer with Co Kα radiation (λ = 1.7089 Å; Co-K$α_1$ and Co-K$α_2$ radiation filter-

ing) with a step size of 0.026° in theta-2theta scan mode in Bragg-Brentano geometry.

Temperature X-ray diffraction (in situ XRD) measurements were done using the AntonPaar HTK1200N chamber installed at MalvernPanalytical Empyrean diffractometer. The temperature range was 300–1200 K with the step of 25 K, the sample was kept in constant high-purity Ar (6N) flow. The measurement procedure was as follows: setting the temperature with a ramp of 5 K min^{-1}, holding the temperature for 10 min. for stabilization, then scanning within 20–80° of 2θ for 20 min. Thermal displacement of the sample surface with respect to the origin of the goniometer was maintained automatically thanks to the motorized sample stage with the appropriate calibration curve.

Thermal properties were examined by differential scanning calorimetry (Netzsch DSC 404 F3) under high purity (99.999%) Ar atmosphere at a constant heating and cooling rate of 10 K min^{-1} with an error of ±2 K.

The microfibers were hot mounted by PolyFast at 453 K and 250 bar. They were ground using 1200, 2400, and 4000 SiC sandpapers and polished further with 1 µm diamond and alumina powder suspensions. Cleaning was performed using isopropanol and followed by air blow fast-drying. Nanoindentation tests were performed with an Agilent G200 Nanoindenter, and the results were analyzed using NanoVision software (Agilent Technologies, USA). The continuous stiffness method (CSM) was employed for the measurements. The following parameters were used for the measurements: Vickers indenter tip surface approach velocity: 10 nm s^{-1}, surface approach distance: 1000 nm, harmonic displacement: 2 nm with 45 Hz frequency, strain rate: 0.05 s^{-1}, and a depth limit of 500 nm indentation was selected. Poisson's ratio was considered to be ≈0.3.[38]

Magnetization as a function of temperature from 300 to 1250 K was measured at ACMIN AGH UST using a LakeShore Model 7407 vibrating sample magnetometer with an oven in an argon atmosphere (purity 99.9995%) with a heating rate of 5 K min^{-1} in the presence at 0.1 T field. The sample was mounted with Thermeez 7020 ceramic putty on a quartz rod. Curie temperatures T_C were estimated as the maximum of the first derivative of the curve.

The shielding of electromagnetic fields was investigated in both the static limit (DC magnetic field shielding for electromagnetic compatibility of devices) and in the microwave frequency range typical of telecommunication systems.

Tubular screens, made of multilayers of $Co_{66}Fe_4Mo_2Si_{16}B_{12}$ microfibers adhered to a nonconductive polystyrene hollow cylinder, were used for static magnetic field shielding measurements. Two designs were tested: one with microfibers aligned parallel to the cylinder's axis (referred to as the vertical configuration) and another where the microfibers wrapped horizontally around the cylinder (horizontal configuration). The tubular constructions have an average inner and outer diameter of 21.4 and 25.3 mm, respectively, with a height of 27.6 mm. A Ga-As Hall probe, positioned at the shield's center, was employed to gauge the magnetic flux density in both axial and transverse field directions. The probe was consistently aligned to measure the magnetic flux density component parallel to the field direction being applied, termed the z-direction.[39,40]

The high-frequency EMI shielding efficiency can be studied in terms of the attenuation constant of electromagnetic radiation
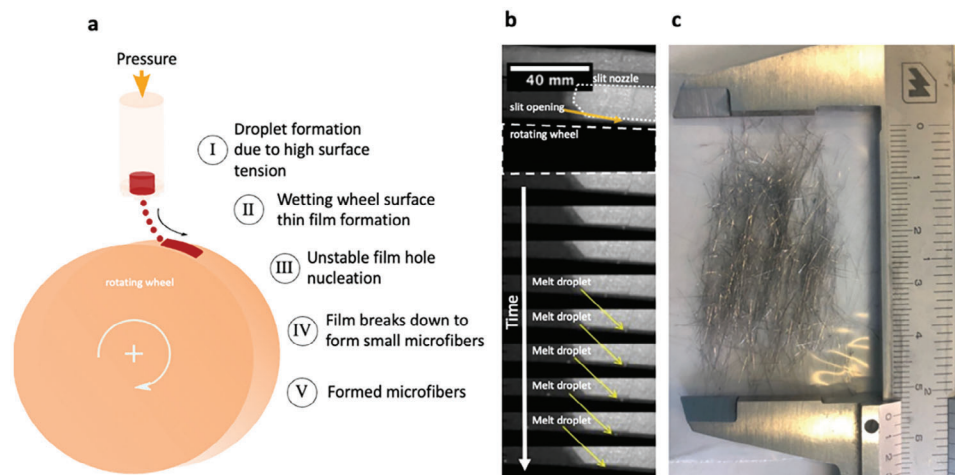
**ADVANCED
SCIENCE NEWS**

www.advancedsciencenews.com

**ADVANCED
ELECTRONIC
MATERIALS**
Open Access

www.advelectronicmat.de

Figure 1. Fabrication of microfibers by modified melt-spinning technique. a) Schematic representation of metal microfiber formation by the modified melt-spinning technique: (I) Droplet formation due to high surface tension (II) Wetting wheel surface thin film formation (III) Unstable film hole nucleation (IV) Film breaks down to form small microfibers (V) Formed microfibers b) Images taken from a high-speed camera movie during the melt-spinning process. c) Fabricated $Fe_{40}Ni_{40}B_{20}$ microfibers. (Part a and b adapted from author's paper,[35] Springer Nature Limited).

that can be computed once the complex relative permittivity ϵ and permeability μ of the composites are known[41] (Equation 1):

$$\alpha = \frac{\sqrt{2}\pi f}{c}\sqrt{(\mu''\varepsilon'' - \mu'\varepsilon') + \sqrt{(\mu''\varepsilon'' - \mu'\varepsilon')^2 + (\mu'\varepsilon'' + \mu''\varepsilon')^2}} \quad (1)$$

The study examined the properties of composite samples, consisting of microfibers embedded in an epoxy matrix (at a wt.% of 25%), in the GHz range. This was accomplished using a cylindrical coaxial cell, known as the EpsiMu toolkit provided by Multiwave Innovation, FR[42]). This cell includes the sample placed between inner and outer conductors, having diameters of 0.56 and 1.3 cm, respectively. This methodology aligns with the procedure outlined by Torsello et al.[43,44] To ensure a consistent 50 Ω impedance and reduce energy loss, the cell features two cone-shaped parts that connect to standard connectors. Once appropriately calibrated, the cell is linked to a ZVK Vector Network Analyzer (manufactured by Rohde & Schwarz GMBH & Co in Munich, Germany). A two-port transmission line technique is then used for analysis. The electromagnetic attributes of the sample are established by a de-embedding process and the Nicolson–Ross–Weir transmission–reflection algorithm.[45,46] Furthermore, based on these properties, the high-frequency conductivity can be determined as described in Equation (2):

$$\sigma = \varepsilon_0\varepsilon''f/2\pi \quad (2)$$

Given the pronounced conductivity and magnetic properties of the microfibers in contrast to the insulating and diamagnetic nature of the polymeric matrix, the characteristics of the composite are predominantly dictated by these inclusions.

3. Results and Discussion

Figure 1a shows the schematic representation of the modified melt-spinning technique for the fabrication of metallic glass

microfibers. In contrast to the conventional planar flow melt-spinning process, in this modified technique no stationary melt puddle is formed and therefore the process is not a continuous ejection of the melt and rather is based on the formation of individual droplets coming through the slit nozzle (visualized in Figure 1b captured by the high-speed camera). Each droplet wets the fast-rotating copper wheel forming a thin film that spontaneously breaks down, and by removal of the heat pull, it solidifies to form the microfibers (see Figure 1c). In fact, the key to this process is the control of surface tension of the melt coming through the slit nozzle that even though it forms the droplets, it has to wet the wheel otherwise instead of microfibers, it solidifies in the forms of particles. Therefore, the melt-spinning parameters such as temperature and pressure are essential for droplet formation, and parameters such as nozzle-to-wheel distance, and wheel speed are controlled to form the thin film on the wheel.

Figure 2a,b shows the scanning electron microscopy images of as-cast $Co_{66}Fe_4Mo_2Si_{16}B_{12}$ metallic glass microfibers. The produced microfibers have rectangular cross-sections; therefore, their size is expressed by two numbers: width and thickness in which their size distribution is presented in Figure 2c–e. What is clear from these figures is that even though the mean value for the thickness and width of the microfibers are ≈5.70 and 42.01 μm (box chart in Figure 2e), the distribution of sizes in Figure 2c,d indicates that the thickness of microfibers is more populated toward 4 μm and their width ≈10 μm. The cross-section view of microfibers is presented in Figure S1 (Supporting Information).

The produced microfibers were analyzed by X-ray diffraction and differential scanning calorimetry to evaluate their crystallinity, and the results are shown in **Figure 3**. Clearly, the produced microfibers have an amorphous structure (Figure 3a). The DSC measurement in Figure 3b shows an endothermic event due to the glass transition followed by another endothermic peak related to the crystallization transformation. The starting temperature of glass transition and crystallization are shown in the curve by T_g and T_x, respectively. The range between the glass
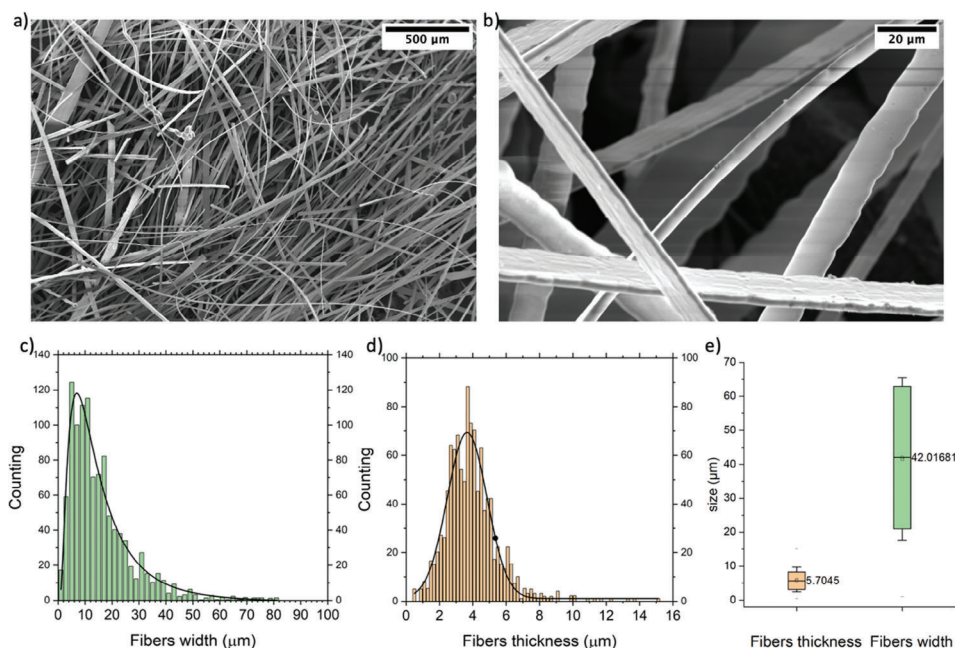
**ADVANCED
SCIENCE NEWS**

www.advancedsciencenews.com

**ADVANCED
ELECTRONIC
MATERIALS**
Open Access

www.advelectronicmat.de

Figure 2. Scanning electron microscopy of $Co_{66}Fe_4Mo_2Si_{16}B_{12}$ metallic glass microfibers a) lower magnification; b) higher magnification; c) size distribution of microfibers width; d) size distribution of microfibers thickness; e) box chart size distribution of width and thickness of microfibers.

transition and the crystallization is named the supercooled liquid region, which indicates the thermal stability of the glassy alloy ($\Delta T_x = T_x - T_g$). The T_g and T_x are estimated to be 834 K, and 867 K, respectively.

The in situ XRD analysis of $Co_{66}Fe_4Si_{16}B_{12}$ alloy is shown in **Figure 4**. According to Figure 4, initially, amorphous $Co_{66}Fe_4Si_{16}B_{12}$ alloy shows no temperature evolution in the collected XRD patterns up to 750 K. At 775 K, reflections originating from the CoSi-like phase (space group $P213$) can be observed. However, those reflections are still overlayed onto broad diffusive pattern originating from atomic disorder. The diffusive pattern vanishes at 825 K, where the CoSi-like phase disappears as well. At this temperature, the sample starts to decompose into several simple crystalline phases including Co ($Fm\bar{3}m$), Si ($Cmca$), Co_3B ($Pnma$), and $B(FeSi)_3$ ($Pnma$). Noticeable, yet small changes oc-

cur at 950 K and 1025 K due to atom diffusion between subsequent phases to form thermodynamically stable compositions. The decomposition is finished at 1000 K, where reflections from the identified phases show no movement or intensity changes.

The microfibers were further characterized for their mechanical properties using the continuous stiffness mode (CSM) of nanoindentation. The typical load-displacement curve obtained from nanoindentation measurement is shown in **Figure 5**. The average hardness and elastic modulus of microfibers were measured to be 11.31 ± 0.60 GPa, and 110.54 ± 11.24 GPa, respectively.

Figure 6a shows the temperature and field dependence of magnetization (M) studied at 0.1 T (1000 Oe). The amorphous structure shows a magnetic signal because the matrix has magnetic nanoparticles. A systematic decrease of magnetization of
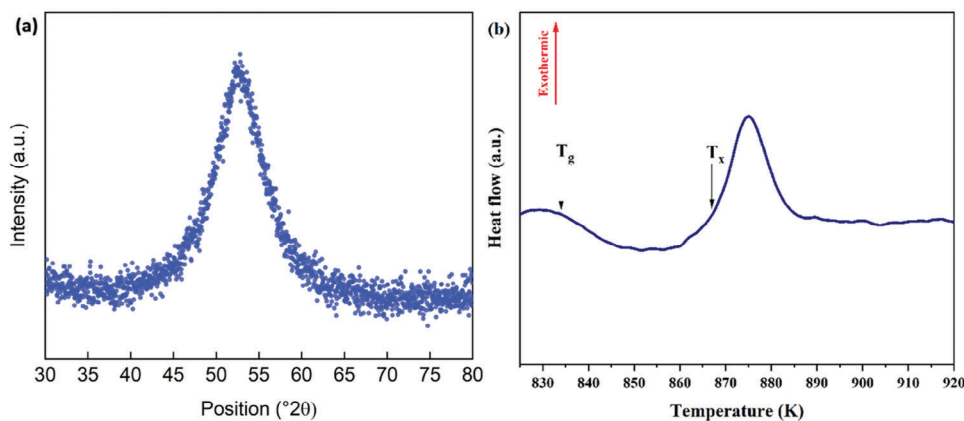

Figure 3. $Co_{66}Fe_4Mo_2Si_{16}B_{12}$ metallic glass microfibers are characterized by a) XRD analysis b) DSC measurement.
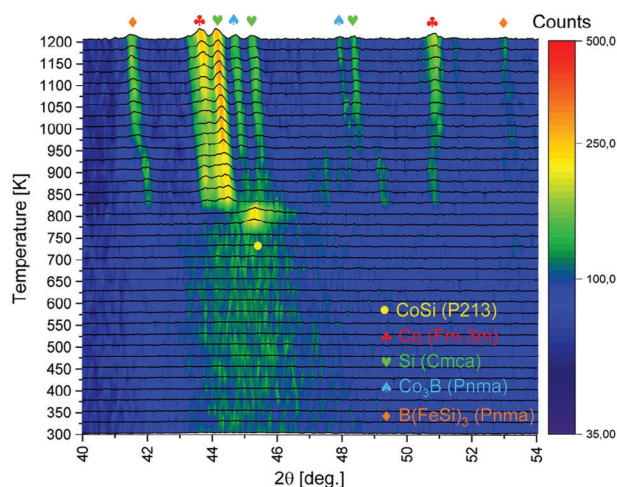
Figure 4. In situ (nonambient) X-ray diffraction of $Co_{66}Fe_4Mo_2Si_{16}B_{12}$ alloy with identified crystalline phases.

the microfibers is observed as a function of increasing temperature from 300 to 550 K. From the derivative, we obtain several peaks responsible for the transformations in the amorphous microfibers. The fitst peak (Figure 6b) close to 508 K corresponds to the Curie temperature of Co_2B, which agrees with the values reported in the literature.[47] We did not notice Co_2B in X-ray diffraction, because they are small nanoparticles. Therefore, we have observed one peak indicating an amorphous phase, while in the magnetic signal, we are able to detect them.

The transition from an amorphous to a crystalline alloy (Figure 6b) started close to 800 K. In **Figure 7a**, an unusual increase in saturation magnetization was observed with temperature from 790 to 850 K. The first step of devitrification was mainly connected with the formation of some crystalline magnetic phases as Co_3B and Co ($Fm\bar{3}m$), which agrees very well with
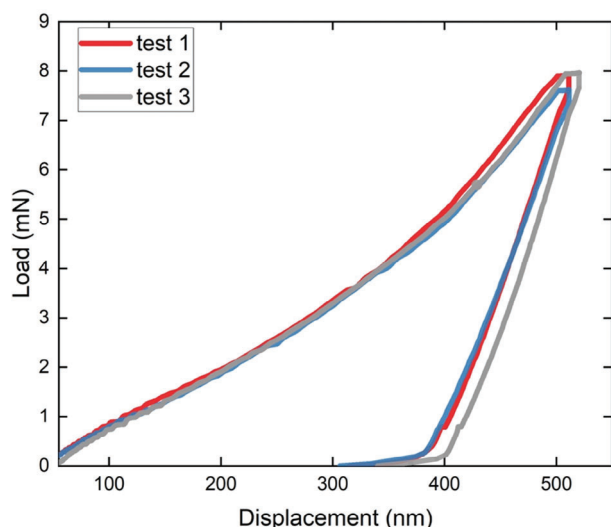
X-ray diffraction (T = 825 K) and DSC measurements (T = 834 K). The crystallization temperature ≈800 K corresponds well with similar data from the literature.[15,48] The Curie temperature for Co_3B is between 700 and 800 K according to the literature.[49] The third peak very well corresponds with XRD diffraction (T = 950 K, and at 1025 K), where possibly an atom diffusion between subsequent phases occurs to form thermodynamically more stable alloys. During cooling, we have observed a peak near 1000 K, typical for this composition.[50] In magnetic measurements, compounds measured in X-ray diffraction, such as CoSi and $B(FeSi)_3$ were not observed. This is due to the fact that in these temperature ranges these compounds do not give a magnetic signal.[51,52]

Figure 7 shows the magnetization against the applied magnetic field hysteresis loop for microfibers before and after annealing at 1250 K. The sample exhibits an ultra-soft magnetic behavior consisting of a hysteresis loop with a saturation magnetization (M_s = 47.7 emu g^{-1}), magnetic field coercivities (H_c = 1 Oe), and magnetic remanence (Mr = 7.9 emu g^{-1}).

Coercivity decreases if the sample gets relaxed, it increases if it gets crystallized. The annealed samples show a higher: saturation magnetization (Ms = 89 emu g^{-1}), magnetic field coercivities (H_c = 38 Oe), and magnetic remanence (Mr = 27.6 emu g^{-1}) compared to the as-cast amorphous samples. This is of course related to the formation of magnetic crystalline phases, which is why all magnetic parameters increase after the annealing process.

We investigated the shielding capability of the microfiber tubes by measuring the magnetic flux density, B_z, in each tube center when increasing the external applied field up to H_{appl} = 65 Oe (**Figure 8a,b**). The shielding factor (SF) was then calculated as the ratio of the applied magnetic field (measured in mT, i.e., $\mu_0 H_{appl}$) to the measured magnetic flux density, B_z.

The analysis highlights the anisotropic behavior of the shielding properties that reflects the microfiber arrangement on the polystyrene hollow cylinder. Indeed, higher shielding performances emerge when the microfiber orientation matches the applied magnetic field direction. In more detail, in the axial field orientation, a shielding factor of about five is achieved in the screens with the microfibers placed in vertical configuration against a maximum SF of about three, shown by the horizontal configuration (Figure 8c). Likewise, in the transverse field orientation, the maximum SF is obtained with the fibers placed in the horizontal configuration (up to eight) whereas the screen attains a maximum SF of about two with the vertical configuration (Figure 8d). Considering that the microfibers are homogeneously distributed, and their amount is the same for both screens, the higher SF reached in transverse field orientation confirms the ability of high-permeability material-based shields' ability to mitigate transverse magnetic fields more effectively than axial ones.[40] In all the cases, above the applied field H_{appl} = 60 Oe, the shielding factor curves can be considered flat and close to unity.

The high-frequency characterization of epoxy-based composites is presented in the first panel of **Figure 9**. The sample exhibits pronounced conductivity due to the metallic inclusions, and a notable increase in the real part of the permittivity compared to the polymeric matrix ($\epsilon' \simeq 3.5$). The decline of σ with rising frequency signifies the metallic nature of the fibers. The attenuation constant of the composite, displayed in the second panel, is roughly 25 times greater than that of the matrix. It peaks at 14 GHz,
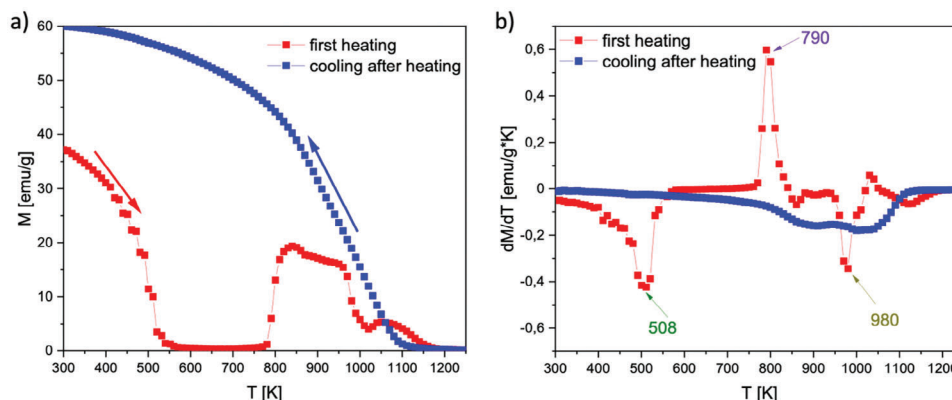

Figure 5. The load-displacement curve on $Co_{66}Fe_4Mo_2Si_{16}B_{12}$ metallic glass microfibers cross-section, measured by continuous stiffness mode of nanoindentation analysis.

ADVANCED
SCIENCE NEWS

www.advancedsciencenews.com

ADVANCED
ELECTRONIC
MATERIALS

www.advelectronicmat.de

Figure 6. The temperature-dependent magnetization at 0.1 T for the amorphous phase a); the derivative of the temperature-dependence used for the determination of the characteristic temperature b) during heating (red) and cooling (blue).

within the Ku frequency band, which is used for satellite communications. Such effective EMI shielding capabilities, coupled with the shape and mechanical attributes of the microfibers, render this system attractive for potential applications. The efficacy of these samples is on par with that of $Fe_{40}Ni_{40}B_{20}$ microfibers[37] (we observe an attenuation coefficient of 631 m^{-1} versus 524 m^{-1} at 8 GHz, situated at the midpoint of the assessed frequency range). This suggests that metallic glasses serve as a feasible option for EMI shielding. Furthermore, the specific composition for these applications can be tailored to fine-tune the mechanical properties as necessitated by the intended use.

4. Conclusion

Herrin, we have fabricated $Co_{66}Fe_4Mo_2Si_{16}B_{12}$ metallic glass microfibers. The amorphous nature of the microfibers was confirmed by XRD and DSC. Based on the DSC analysis, T_g and T_x are estimated to be 834 K, and 867 K, respectively. Mechanical properties of the microfibers were investigated using the continuous stiffness mode of Nanoindentation and have shown a very high hardness in the range of 11.31 ± 0.60 GPa, and an elastic modulus (E) of 110.54 ± 11.24 GPa.

Based on the magnetic characterizations and the in situ XRD results, we can conclude that at the beginning, the sample con-

tains magnetic nanoparticles (Co_2B) in an amorphous matrix, and the subsequent annealing of the microfibers results in crystalline phases according to the scheme:

Amorphous → CoSi → Si + α-Co + Co_3B + B(FeSi)$_3$
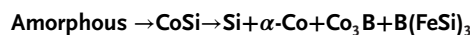
Regarding the EMI shielding properties:

- In the static regime, the shielding factor reaches five and has a clear anisotropy.
- At GHz frequencies, observed a substantial up to 25-fold increase in the attenuation constant within the Ku frequency band.

The combination of mechanical strength and electromagnetic shielding capabilities positions this system as promising for EMI shielding applications, particularly in complex geometries.

Supporting Information

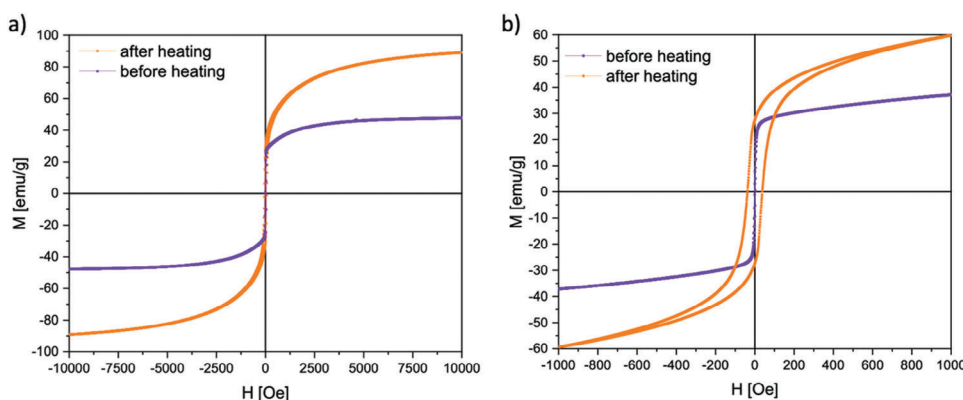Supporting Information is available from the Wiley Online Library or from the author.

Figure 7. The isothermal magnetization curves at 300 K (a) before (violet) and after heating (orange). a) at a high magnetic field, H = −10 000 to 10,000 Oe; b) at a low magnetic field, H = −1000 to 1000 Oe.

2300490 (7 of 9)

**ADVANCED
SCIENCE NEWS**

www.advancedsciencenews.com

**ADVANCED
ELECTRONIC
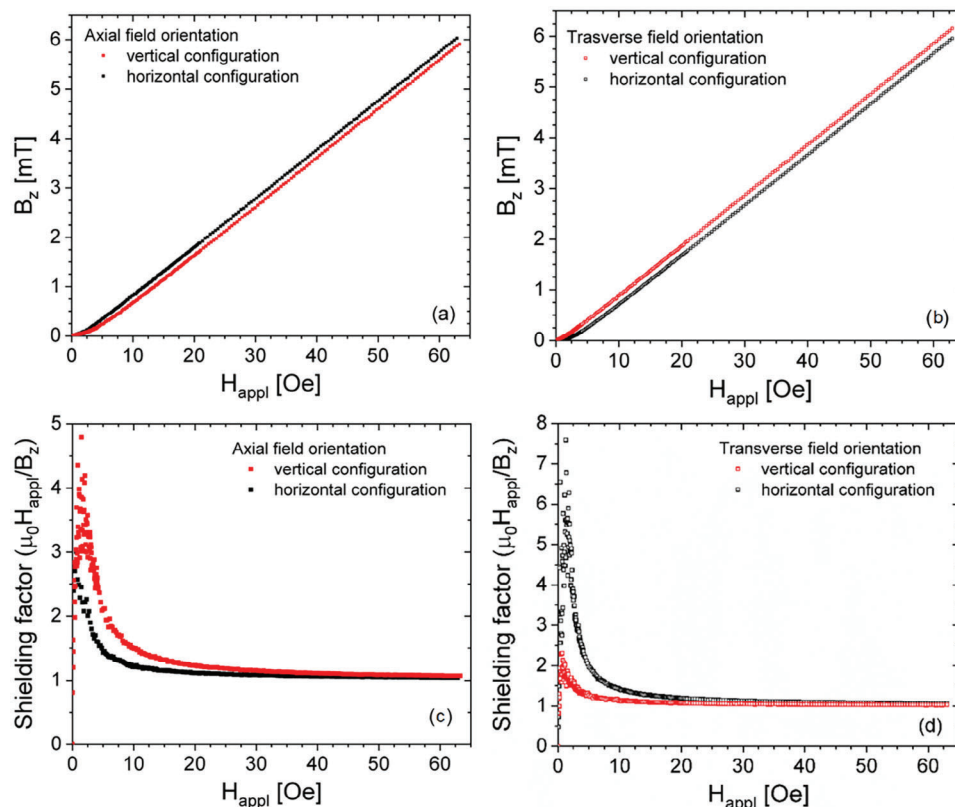MATERIALS**
Open Access

www.advelectronicmat.de

Figure 8. Magnetic flux density was measured by the Hall probe positioned at the center of the tubular shields in both axial a) and transversal b) field orientation. The corresponding shielding factor is plotted in panels c) and d).
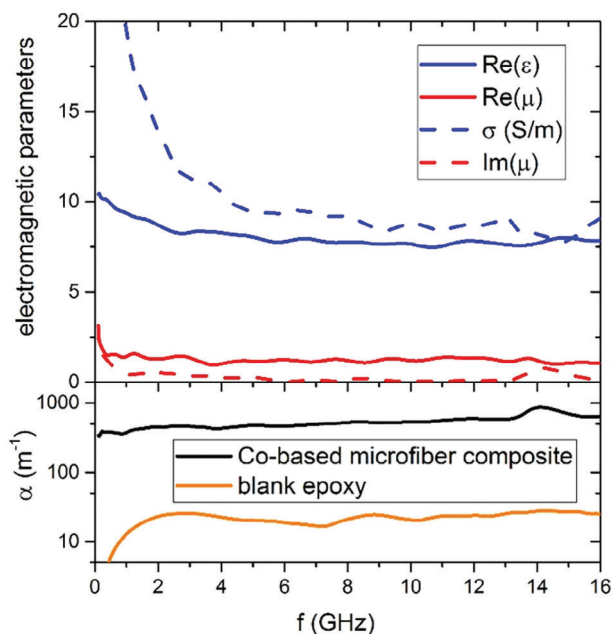

Figure 9. Top panel: high-frequency electromagnetic properties of the Co-based microfiber samples embedded in an epoxy matrix. Bottom panel: attenuation coefficient of electromagnetic radiation of the composite sample (black) compared to the blank epoxy matrix (orange).

Acknowledgements

Conflict of Interest

The authors declare no conflict of interest.

Author Contributions

E.S. contributed to the conceptualization, methodology, writing original draft, and acquiring funding; A.Ż. contributed to magnetic measurements; T.K. contributed to the metallic microfiber fabrication; P.B. contributed to methodology, validation, and reviewing the manuscript; L.G. (Gondek) contributed to magnetic measurement analysis and their data validation; R.R. contributed to methodology and writing original draft; D.T., G.G., and R.G. contributed to high-frequency characterization, to the discussion and to the writing of the manuscript; M.F., and L.G. contributed to magnetic shielding measurements, to the discussion and to the writing of the manuscript.

2300490 (8 of 9)

Data Availability Statement

The data that support the findings of this study are available from the corresponding author upon reasonable request.

[1] A. Inoue, B. Shen, H. Koshiba, H. Kato, A. R. Yavari, *Nat. Mater.* **2003**, *2*, 661.

[2] A. V. Nosenko, V. V. Kyrylchuk, M. P. Semen'ko, M. Nowicki, A. Marusenkov, T. M. Mika, O. M. Semyrga, G. M. Zelinska, V. K. Nosenko, *J. Magn. Magn. Mater.* **2020**, *515*, 167328.

[3] S. Wu, S. Chen, J. Ouyang, C. Zuo, L. Yu, X. Yang, *J. Phys. Conf. Ser.* **2011**, *263*, 012012.

[4] H. Zheng, W. Yao, H. Sun, G. Tong, *J. Magn. Magn. Mater.* **2018**, *468*, 109.

[5] H. Sun, Q. Man, Y. Dong, B. Shen, H. Kimura, A. Makino, A. Inoue, *J. Appl. Phys.* **2010**, *107*, 09A319.

[6] H. Sun, F. Q. Guo, D. Z. Wang, *J. Clin. Neurol.* **2010**, *23*, 31.

[7] V. K. Nosenko, V. V. Maslov, A. P. Kochkubey, V. V. Kirilchuk, *J. Phys. Conf. Ser.* **2008**, *98*, 072006.

[8] I. B. Kekalo, P. S. Mogil'nikov, *Tech. Phys.* **2015**, *60*, 1815.

[9] N. A. Skulkina, O. A. Ivanov, A. K. Mazeeva, P. A. Kuznetsov, V. I. Chekis, N. D. Denisov, *Phys. Met. Metallogr.* **2018**, *119*, 1154.

[10] N. A. Skulkina, A. K. Mazeeva, P. A. Kuznetsov, N. D. Denisov, V. I. Chekis, *J. Magn. Magn. Mater.* **2020**, *502*, 166529.

[11] G. Aguilar-Sahagun, P. Quintana, E. Amano, J. T. S. Irvine, R. Valenzuela, *J. Appl. Phys.* **1998**, *75*, 7000.

[12] I. Betancourt, M. Jiménez, S. Aburto, V. Marquina, R. Gómez, M. L. Marquina, R. Ridaura, R. Miki, R. Valenzuela, *J. Magn. Magn. Mater.* **1995**, *140–144*, 459.

[13] G. Buttino, A. Cecchetti, M. Poppi, *J. Magn. Magn. Mater.* **1997**, *172*, 147.

[14] G. Bordin, G. Buttino, A. Cecchetti, M. Poppi, *J. Phys. D. Appl. Phys.* **1997**, *30*, 2163.

[15] J. Swierczek, H. Lampa, Z. Nitkiewicz, Z. Balaga, *Mater. Sci. Eng. A* **2003**, *356*, 108.

[16] L. Omana, A. Chandran, R. E. John, R. Wilson, K. C. George, N. V. Unnikrishnan, S. S. Varghese, G. George, S. M. Simon, I. Paul, *ACS Omega* **2022**, *7*, 25921.

[17] N. Maruthi, M. Faisal, N. Raghavendra, *Synth. Met.* **2021**, *272*, 116664.

[18] S. H. Lee, S. Yu, F. Shahzad, J. P. Hong, W. N. Kim, C. Park, S. M. Hong, C. M. Koo, *Compos. Sci. Technol.* **2017**, *144*, 57.

[19] S. Maiti, N. K. Shrivastava, S. Suin, B. B. Khatua, *ACS Appl. Mater. Interfaces* **2013**, *5*, 4712.

[20] D.-X. Yan, H. Pang, B. Li, R. Vajtai, L. Xu, P.-G. Ren, J.-H. Wang, Z.-M. Li, *Adv. Funct. Mater.* **2015**, *25*, 559.

[21] Z. Ma, J. Li, J. Zhang, A. He, Y. Dong, G. Tan, M. Ning, Q. Man, X. Liu, *J. Mater. Sci. Technol.* **2021**, *81*, 43.

[22] M. Stoppa, A. Chiolerio, *Sensors (Switzerland)* **2014**, *14*, 11957.

[23] A. E. Markaki, T. W. Clyne, *Biomaterials* **2004**, *25*, 4805.

[24] R. Liu, X. Wang, J. Liu, Y. Zhang, G. Cao, Z. Liu, G. Qu, Z. Li, M. Zhang, *J. Mater. Res. Technol.* **2021**, *14*, 1390.

[25] J. Yi, X. X. Xia, D. Q. Zhao, M. X. Pan, H. Y. Bai, W. H. Wang, *Adv. Eng. Mater.* **2010**, *12*, 1117.

[26] K. S. Nakayama, Y. Yokoyama, T. Wada, N. Chen, A. Inoue, *Nano Lett.* **2012**, *12*, 2404.

[27] Y. Ma, H. Wang, W. Lv, S. Ji, B. G. Pollet, S. Li, R. Wang, *RSC Adv.* **2015**, *5*, 68655.

[28] J. Li, G. Doubek, L. Mcmillon-Brown, A. D. Taylor, *Adv. Mater.* **2019**, *31*, 1970050.

[29] V. S. Larin, A. V. Torcunov, A. Zhukov, J. González, M. Vazquez, L. Panina, *J. Magn. Magn. Mater.* **2002**, *249*, 39.

[30] V. Zhukova, M. Ipatov, A. Zhukov, J. Gonzalez, J. Blanco, *Sensors Act. B Chem* **2007**, *126*, 232.

[31] G. Villanueva, A. García-Gómez, J. María Blanco, P. Corte-León, M. Ipatov, Á. González, J. González, A. Zhukov, V. Zhukova, *Sensors* **2023**, *23*, 8068.

[32] P. Corte-León, V. Zhukova, M. Ipatov, J. M. Blanco, J. González, A. Zhukov, *AIP Adv.* **2019**, *9*, 35017.

[33] A. Zhukov, P. Corte-León, L. González-Legarreta, M. Ipatov, A. Talaat, J. M. Blanco, J. Gonzalez, V. Zhukova, *Adv. Mater. Lett.* **2019**, *10*, 305.

[34] M. Salaheldeen, A. Talaat, M. Ipatov, V. Zhukova, A. Zhukov, *Process.* **2022** **2022**, *10*, 2248.

[35] E. Sharifikolouei, B. Sarac, Y. Zheng, P. Bala, J. Eckert, *Sci. Rep.* **2022**, *12*, 10784.

[36] E. Sharifikolouei, B. Sarac, A. Micoulet, R. Mager, M. Watari-Alvarez, E. Hadjixenophontos, Z. Burghard, G. Schmitz, J. P. Spatz, *Mater. Des.* **2022**, *223*, 111242.

[37] E. Sharifikolouei, A. Zywczak, B. Sarac, T. Koziel, R. Rashidi, P. Bala, M. Fracasso, R. Gerbaldo, G. Ghigo, L. Gozzelino, D. Torsello, *Adv. Electron. Mater.* **2023**, 2300178.

[38] A. Kuś, W. Pilarczyk, A. Małachowska, A. Ambroziak, P. Gębara, *Mater* **2021**, *14*, 7357.

[39] L. Gozzelino, R. Gerbaldo, G. Ghigo, F. Laviano, D. Torsello, V. Bonino, M. Truccato, D. Batalu, M. A. Grigoroscuta, M. Burdusel, G. V. Aldica, P. Badica, *Supercond. Sci. Technol.* **2019**, *32*, 034004.

[40] L. Gozzelino, M. Fracasso, M. Solovyov, F. Gömöry, A. Napolitano, R. Gerbaldo, G. Ghigo, F. Laviano, D. Torsello, M. A. Grigoroscuta, G. Aldica, M. Burdusel, P. Badica, *Supercond. Sci. Technol.* **2022**, *35*, 044002.

[41] B. Zhao, G. Shao, B. Fan, W. Zhao, Y. Chen, R. Zhang, *RSC Adv.* **2015**, *5*, 9806.

[42] D. Ba, P. Sabouroux, *Microw. Opt. Technol. Lett.* **2010**, *52*, 2643.

[43] D. Torsello, G. Ghigo, M. Giorcelli, M. Bartoli, M. Rovere, A. Tagliaferro, *Carbon Trends* **2021**, *4*, 100062.

[44] D. Torsello, M. Bartoli, M. Giorcelli, M. Rovere, R. Arrigo, G. Malucelli, A. Tagliaferro, G. Ghigo, *Nanomater* **2021**, *11*, 2383.

[45] A. M. Nicolson, G. F. Ross, *IEEE Trans. Instrum. Meas.* **1970**, *19*, 377.

[46] J. Baker-Jarvis, E. J. Vanzura, W. A. Kissick, *IEEE Trans. Microw. Theory Tech.* **1990**, *38*, 1096.

[47] A. Edström, M. Werwiński, D. Iuşan, J. Rusz, O. Eriksson, K. P. Skokov, I. A. Radulov, S. Ener, M. D. Kuz'Min, J. Hong, M. Fries, D. Y. Karpenkov, O. Gutfleisch, P. Toson, J. Fidler, *Phys. Rev. B – Condens. Matter Mater. Phys.* **2015**, *92*, 174413.

[48] X. Zhou, R. Liu, H. Zhou, *J. Magn. Magn. Mater.* **2020**, *493*, 165729.

[49] A.-M. Zieschang, J. D. Bocarsly, J. Schuch, C. V. Reichel, B. Kaiser, W. Jaegermann, R. Seshadri, B. Albert, *Inorg. Chem.* **2019**, *58*, 16609.

[50] Y. Nykyruy, S. Mudry, I. Shtablavyi, Y. Tsekhmister, I. Gnilitskyi, *Mater. Chem. Phys.* **2022**, *287*, 126317.

[51] N. E. Sluchanko, V. V. Glushkov, S. V. Demishev, A. A. Menovsky, L. Weckhuysen, V. V. Moshchalkov, *Phys. Rev. B* **2002**, *65*, 064404.

[52] K. Seo, K. S. K. Varadwaj, P. Mohanty, S. Lee, Y. Jo, M.-H. Jung, J. Kim, B. Kim, *Nano Lett.* **2007**, *7*, 1240.